JOURNAL OF PROPULSION AND POWER
Vol. 11, No. 5, September–October 1995

Comparison Between Numerically Modeled and Experimentally Measured Wave-Rotor Loss Mechanisms

Daniel E. Paxson*
NASA Lewis Research Center, Cleveland, Ohio 44135

A numerical model has been developed that is capable of predicting the performance of a wave-rotor (pressure exchanger) of specified geometry over a wide range of operating conditions. The model can account for the major loss mechanisms of leakage from the tube ends, fluid viscosity, heat transfer to the tube walls, finite tube opening time, shock waves, and nonuniform port flows. It is a one-dimensional flow model that follows a single tube as it rotates past the various stationary ports. Since the model is relatively simple (i.e., one dimensional), it uses little computer time. This makes it suitable for design as well as analytical purposes. This article will present a brief description of the model and then discuss a comparison between the model predictions and several wave-rotor experiments.

I. Introduction

THE wave-rotor represents a promising technology for achieving high overall pressure ratios and peak cycle temperatures in future gas-turbine engines. Shown schematically in Fig. 1, the wave-rotor is a device that utilizes unsteady waves to transfer energy to and from the working fluid passing through it. Detailed descriptions of the principles of operations may be found in numerous references[1–6] and will not be presented here.

In order to correctly design or predict the performance of a wave-rotor it is necessary to account not only for the unsteady wave processes that are usually assumed to govern the machine, but also for some of the major loss mechanisms that exist. These include leakage from the ends of the wave-rotor passages to the cavity in which they rotate (Fig. 2), viscous losses, heat transfer from the passage walls to the gas, and losses induced by the finite opening time of the tubes as they enter and leave the ports. It has been consistently shown in experiments[7–9] that machines designed without these losses considered, perform substantially worse than the idealized predictions. Several multidimensional numerical studies[10–12] have been conducted in order to examine the complex fluid mechanics associated with these as well as other losses. An effort is under way by the author, however, to develop a numerical model that can appraise these major losses, but that is simple enough to be used for rapid, general design, and analysis. This article will provide a description of this model as well as comparisons between the model predictions and three wave-rotor experiments that have been or are being performed.[7–9] It is noted that some of the model description has been reported previously,[13] and as such will be suitably abbreviated here.

II. Model Description

The model numerically integrates the equations of motion in a single passage as it rotates past the various ports and walls that comprise the ends of the wave-rotor. These ports (and walls) establish the boundary conditions for the governing equations in the passage. Ports are specified by their angular location relative to some fixed point on the wave-rotor and by a representative pressure and temperature. Up to six ports may be specified on the present model (three per side). With each time step the passage advances an angular distance specified by the angular velocity. If the flow is into the passage, the pressure and temperature are interpreted as stagnation values. If the flow is out of the passage, only the port pressure is required, and it is interpreted as a static value. Determination of the direction of the flow at each time step is somewhat difficult and is discussed in Sec. II.B as well as in Refs. 6 and 13.

The governing equations may be written as

$$\frac{\partial \underline{w}}{\partial t} + \frac{\partial \underline{F}(\underline{w})}{\partial x} = \underline{S}(\underline{w}) \tag{1}$$

where the vectors $\underline{w}$ and $\underline{F}$ have the respective perfect gas forms:

$$\underline{w} = \begin{Bmatrix} \rho \\ \rho u \\ \left[\dfrac{p}{\gamma(\gamma-1)} + \dfrac{\rho u^2}{2}\right] \end{Bmatrix} \tag{2}$$

$$\underline{F} = \begin{Bmatrix} \rho u \\ \dfrac{p}{\gamma} + \rho u^2 \\ u\left[\dfrac{p}{(\gamma-1)} + \dfrac{\rho u^2}{2}\right] \end{Bmatrix} \tag{3}$$

Here, γ is the ratio of specific heats. These equations have been nondimensionalized using a reference state p^*, ρ^*, and a^*, where a^* is the speed of sound. The distance has been scaled by the passage length L and the time has been scaled using the wave transit time L/a^*. The form of the source vector $\underline{S}(\underline{w})$ will be discussed in Sec. II.A. Equation (1) is integrated numerically using the following technique:

$$\underline{w}_i^{n+1} = \underline{w}_i^n - (\underline{f}_{i+1/2}^n - \underline{f}_{i-1/2}^n)(\Delta t/\Delta x) + \underline{s}_i^n \Delta t \tag{4}$$

Presented as Paper 93-2522 at the AIAA/SAE/ASME/ASEE 29th Joint Propulsion Conference, Monterey, CA, June 28–30, 1993; received Oct. 22, 1993; revision received March 23, 1995; accepted for publication March 31, 1995.

*Aerospace Engineer, System Dynamics Branch, M/S 77-1. Member AIAA.

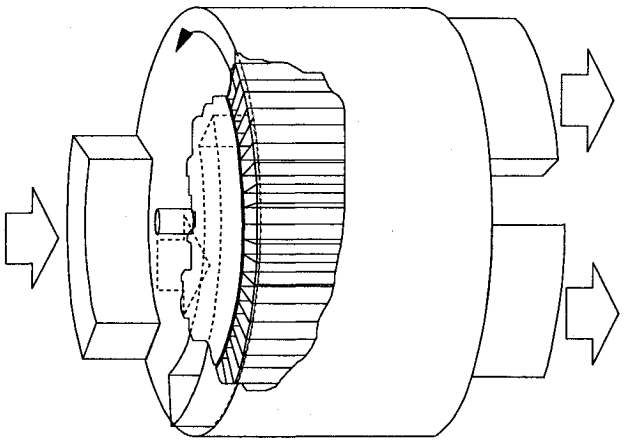

Fig. 1 Wave-rotor schematic.

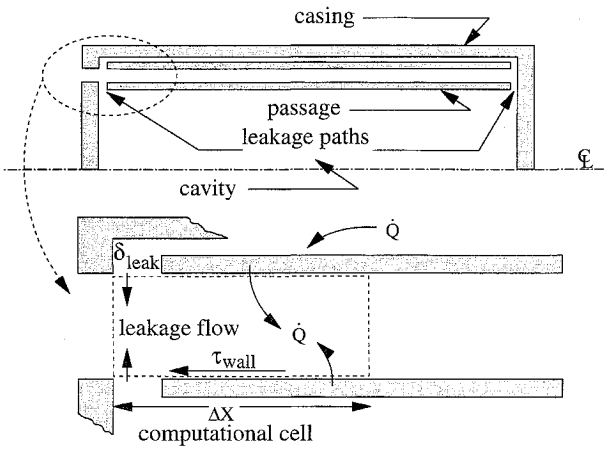

Fig. 2 Source term contributions.

where the numerical flux estimate $\underline{f}^n_{i+1/2}$ is

$$\underline{f}^n_{i+1/2} = \frac{\underline{F}^n_{i+1} + \underline{F}^n_i}{2} - \frac{1}{2}\underline{\Phi}^{\text{Roe}}_{i+1/2} + \frac{\Delta t}{4}\left([A]^n_{i+1}\underline{S}^n_{i+1} - [A]^n_i\underline{S}^n_i\right) \tag{5}$$

and the numerical source $\underline{s}^n_i$ is

$$\underline{s}^n_i = \tfrac{1}{2}(3\underline{S}^n_i - \underline{S}^{n-1}_i) \tag{6}$$

The term $\underline{\Phi}^{\text{Roe}}$ in Eq. (5) refers to the flux-limited dissipation based on Roe's[14] approximate Riemann solver for Eq. (1) without a source vector. The matrix $[A]$ is the Jacobian of the flux vector $\underline{F}$. The superscript n indicates the discrete temporal index $n\Delta t$, and the subscript i indicates the spatial index $i\Delta x$. This scheme has the advantage of being formally second-order accurate in time and space when the flow is smooth, yet maintaining the high resolution of Roe's method in the vicinity of shock waves. Furthermore, as the source strength approaches zero, the scheme becomes monotonic, which is physically correct. Equation (4) is also conservative in the sense that when summed over the index i, an approximation to integration, the only changes to the conserved vector arise from the fluxes at the ends and the source terms (this is not the case for the scheme described in Ref. 13).

A. Source Terms

There are three effects presently modeled that contribute to the source vector. These are 1) viscous effects, 2) heat transfer from the passage walls to the working fluid, and 3) leakage from the passage to the wave-rotor cavity. These effects are illustrated in Fig. 2 and will be discussed later.

1. *Viscous Source Term*

For a one-dimensional model, viscous effects are manifested as a wall shear stress or skin friction factor c_f. An estimate has been obtained in the present model by assuming that the friction factor is some function of the local Reynolds number Re in the computational cell. The relevant length scale for the unsteady flow in the passage is the height of the boundary layer δ. This height may be estimated using the analogy of a suddenly accelerated plate (i.e., Stokes' first problem) as

$$\delta = \sqrt{\nu^* L/a^*} \tag{7}$$

where ν^* is the kinematic viscosity at the reference state (the dynamic viscosity is assumed constant). Although many possibilities exist for the functionality of the friction factor, the present model assumes that it is proportional to the Reynolds number raised to some power, i.e.,

$$c_f \equiv \tau_{\text{wall}}/\rho u^2 = \alpha Re_\delta^{-j} \tag{8}$$

From the data collected thus far, the best value for j appears to be one-half. The values of α for the three experiments studied are listed in Table 1. These were found to yield the best match to the data. It is encouraging to note that they are all nearly the same. The one-dimensional model described in Ref. 5 used a value of $j = 0$; however, when this was attempted in the present model it was found that, in order to correctly match data, α had to be varied substantially between experiments and even within them. Thus, the nondimensional viscous source term of Eq. (1) takes the form

$$s_2 = \sigma_2 u\sqrt{\rho|u|}$$
$$\sigma_2 \equiv -4\alpha\left(\frac{L}{D_h}\right)^{1/2}\left(\frac{\sqrt{\nu^* L/a^*}}{D_h}\right)^{1/2} \tag{9}$$

where D_h is the passage hydraulic diameter.

2. *Heat Transfer Source Term*

Heat transfer is assumed to occur only between the working fluid and the upper and lower walls of the passage. No passage-to-passage heat transfer is accounted for. It is also assumed that no conduction of heat occurs along the passage walls (i.e., the x direction). The Reynolds–Colburn analogy[15] is used to calculate the heat transfer coefficient from the skin friction coefficient of Eq. (8). The resulting source term is

$$s_3^{\text{ht}} = \sigma_3^{\text{ht}}\sqrt{\rho|u|}(T - T_{\text{wall}})$$
$$\sigma_3^{\text{ht}} \equiv [\sigma_2/(\gamma - 1)](D_h/2h)Pr^{-2/3} \tag{10}$$

where Pr is the Prandtl number, h is the passage height, and T and T_{wall} are the gas and wall temperatures, respectively,

Table 1 Experimental parameters

	Ref. 9	Ref. 7	Ref. 8
L	0.46 m	0.28	0.30
R	15.0 cm	7.4	5.8
Passages	130	30	36
h	1.02 cm	5.59	2.31
δ_{leak}	Variable	0.018 cm	0.064
Speed	4000 rpm	6000	19,000
Inlet total pressure	0.207 MPa	Variable	0.101
Inlet total temperature	~333 K	308	283
Exit static pressure	Low: Variable High: Variable	Low: 0.101 MPa High: Variable	0.101
Cycles/revolution	1	3	1
C_D, Eq. (13)	0.5	0.5	0.47
α, Eq. (9)	0.1374	0.1266	0.1319

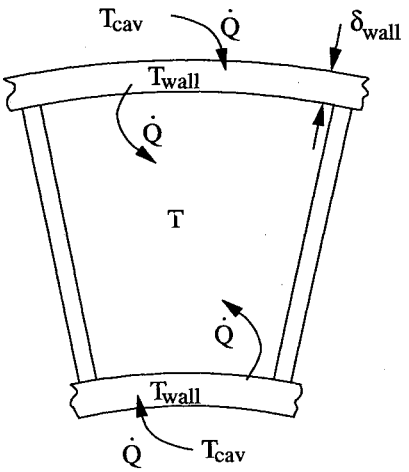

Fig. 3 Wall heat flow path schematic.

for the computational cell scaled by the reference temperature T^*.

A lumped capacitance technique is used to track the temperature of the wall. Referring to Fig. 3, the governing equation for any discrete section may be written in nondimensional form as

$$\frac{dT_{wall}}{dt} = -\phi_1 s_3^{ht} + \phi_2(T_{cav} - T_{wall})$$

$$\phi_1 = \frac{\gamma - 1}{2}\left(\frac{h}{\delta_{wall}}\right)\left(\frac{1}{\rho_{wall}}\right)\left(\frac{c_p}{c_{wall}}\right)$$

$$\phi_2 = 0.02Pr^{-0.4}\left(\frac{L}{\delta_{wall}}\right)\left(\frac{c_p}{c_{wall}}\right)\left(\frac{a^*R}{\nu^*}\right)^{-0.2} \times \left(\frac{1}{\rho_{wall}}\right)\left(\frac{\rho_{cav}\omega R}{a^*}\right)^{0.8} \tag{11}$$

Here, δ_{wall}, c_{wall}, and ρ_{wall} are the wall thickness, specific heat, and nondimensional density, respectively; c_p is the gas specific heat at constant pressure, R is the rotor radius, ρ_{cav} is the nondimensional cavity density, and ω is the rotor speed. The cofficient ϕ_2 is the product of the Fourier and Biot moduli[15] for the outer surface of the wall. The heat transfer coefficient in ϕ_2 was derived from a correlation for steady turbulent flow over a flat plate[16] with the flat plate length replaced with the rotor circumference. Analysis has indicated that the time constants associated with transients in the wall temperature and those in the cavity (Fig. 2) are much larger than the wave transit time or even the time for one complete wave cycle. Thus, the wall temperature distribution (and the state of the cavity) is assumed constant for one wave-rotor cycle and Eq. (11) is integrated using simple Euler integration as

$$T_{wall_i}^{t+t_{cycle}} = T_{wall_i}^{t} + \sum_{n=0}^{t_{cycle}/\Delta t} -\phi_1 s_{3_i}^{ht}\Delta t + \phi_2 t_{cycle}(T_{cav}^{t} - T_{wall_i}^{t}) \tag{12}$$

In practice (for steady-state results), a much smaller wall thickness than the actual value is used in ϕ_1 and ϕ_2 (about 1/100th). This speeds convergence of the wall temperature distribution.

3. Leakage Source Term

Since leakage occurs only at the ends of the wave-rotor passage, the leakage source terms are only added to the first and last computational cells of the model (not the image cells used for implementing boundary conditions). Only leakage to and from the cavity is modeled. Leakage from one passage to another is neglected. The leakage at each end is assumed to occur in the manner of an isentropic, steady-flow orifice that has an area equal to twice the product of the leakage gap δ_{leak} and the passage width b. The leakage affects both the continuity and energy equations of the vector Eq. (1). The nondimensional form of these sources may be written as

$$s_1^1 = \sigma_1^1\sqrt{p\rho}f(p_{cav}/p)$$
$$\sigma_1^1 \equiv -C_D\sqrt{2/(\gamma - 1)}(\delta_{leak}/h\Delta x) \tag{13}$$

$$s_3^1 = \sigma_3^1\sqrt{p\rho}f(p_{cav}/p)$$
$$\sigma_3^1 \equiv \sigma_1^1/(\gamma - 1) \tag{14}$$

Here, T_0 is the nondimensional stagnation temperature, and C_D is the discharge coefficient. The function f is St. Venant's orifice equation[17] defined by

$$f = \sqrt{\left(\frac{p_{cav}}{p}\right)^{2/\gamma} - \left(\frac{p_{cav}}{p}\right)^{(\gamma+1)/\gamma}}, \qquad \frac{p_{cav}}{p} > \left(\frac{2}{\gamma + 1}\right)^{\gamma/(\gamma-1)} \tag{15}$$

or

$$f = \sqrt{\left(\frac{2}{\gamma + 1}\right)^{2/(\gamma-1)} - \left(\frac{2}{\gamma + 1}\right)^{(\gamma+1)/(\gamma-1)}}$$
$$\frac{p_{cav}}{p} < \left(\frac{2}{\gamma + 1}\right)^{\gamma/(\gamma-1)}$$

If the cavity pressure is greater than cell pressure then the pressure ratio in Eq. (15) is inverted, the sign of f changes, and p, ρ, T_0 become those of the cavity. Note that those cells with leakage have two contributions to the energy equation source term, one from Eq. (10) and one from Eq. (14).

Like the wall temperatures, the cavity state is assumed constant over the period of one cycle and is updated using Euler integration of the continuity and energy equations written as

$$\rho_{cav}^{t+t_{cycle}} = \rho_{cav}^{t} - \left(\frac{RhL}{V_{cav}}\right)\Delta x\Delta t\theta_p \sum_{n=0}^{t_{cycle}/\Delta t}([s_1^1]_{left}^n + [s_1^1]_{right}^n) \tag{16}$$

$$p_{cav}^{t+t_{cycle}} = p_{cav}^{t} - \left(\frac{RhL}{V_{cav}}\right)\Delta x\theta_p\left\{\sum_{n=0}^{t_{cycle}/\Delta t}\gamma(\gamma - 1)([s_3^1]_{left}^n + [s_3^1]_{right}^n)\Delta t - t_{cycle}\phi_3\sum_{i=0}^{N}(T_{wall_i} - T_{cav})\right\} \tag{17}$$

where

$$\phi_3 = 0.04Pr^{-0.4}\gamma\left(\frac{L}{h}\right)\left(\frac{a^*R}{\nu^*}\right)^{-0.2}\left(\frac{\rho_{cav}\omega R}{a^*}\right)^{0.8} \tag{18}$$

θ_p is the angular passage width, N is the number of computational cells, and V_{cav} is the cavity volume.

B. Boundary Conditions: Flow Direction and Finite Opening Time

The implementation of appropriate boundary conditions has been discussed in detail in Refs. 6 and 13. Briefly, there are two major complications to be dealt with. The first is that the wave-rotor model must be able to calculate the flowfield in the passage for any specified set of ports and port conditions. This means that it must be capable of marching in time

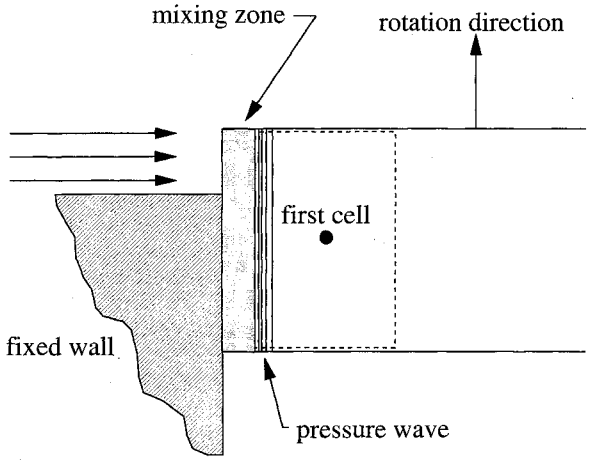

Fig. 4 Finite opening time.

regardless of the direction of the flows at the ends. The second complication of applying boundary conditions arises from the fact that as a passage enters or leaves the vicinity of a port, a period of time exists when the passage end is only partially open. This is shown in Fig. 4 for the case of inflow. This effect, sometimes referred to as finite opening time, can substantially influence the dominant wave speeds.

Considering first the flow direction problem, hyperbolic equations such as (1) have very different boundary requirements for inflow and outflow. These requirements relate to the characteristic, or directional nature of the governing equations. At any boundary, some flow information must come from outside the computing domain and some must be extracted from within. If, for instance, the flow is out of the passage, then only one piece of outside information is required. Typically, this is the static pressure. If the flow is inward, then two pieces of outside data are needed. If inflow boundary conditions are specified for a flow that is actually outward, then the problem is ill-posed and errors (usually catastrophic) result. At each time step then, the model must somehow "look ahead," determine the direction of the flow, and supply the requisite information. In practice, this is achieved as follows. At any port, the flow is assumed to be outward and the specified pressure is interpreted to be static. This information, together with the state of the interior computational cell adjacent to the boundary is enough to solve for the velocity and density across the single wave, which is assumed to be traveling into the computing space (i.e., at the boundary). If the velocity is indeed outward, then the problem is solved and the calculated pressure, density, and velocity are assigned to the image cell (a fictitious computational cell outside the computing domain). If the calculated velocity is inward, then the initial assumption was incorrect. At this point the boundary problem is restarted, assuming inflow and with the specified temperature and pressure interpreted as stagnation values. Assuming the flow in the port is isentropic and steady, the port stagnation conditions and the adjacent interior computational cell state (and a Mach number if the flow is supersonic) uniquely determine the two waves that travel into the computing space, and thus, the state of the image cell.

The finite opening time effect is accounted for in the model as follows. For inflow, the port zone is again assumed isentropic and steady with specified stagnation conditions. It is connected to a fictitious steady mixing zone by way of a converging nozzle with throat area equal to that of the partially open end of the passage. In the mixing zone the fluid is assumed to expand to the full area of the passage and to a uniform state. Adjacent to the mixing zone is the first interior computing cell in which the state is known. A guess is made for the exit pressure of the "nozzle" throat. This uniquely determines the state of the fluid at the exit of the mixing zone. The pressure at the end of the mixing zone, together with the state of the first computing cell determine the velocity across the two characteristic waves that are traveling into the passage. This velocity must match that at the end of the mixing zone. If it does not, then a new guess must be made for the throat exit pressure. This process is repeated iteratively until the velocities match. At this point the computed pressure, density, and velocity at the exit of the mixing zone are assigned to the image cell. For outflow the specified port pressure is assumed static. Now the mixing zone of Fig. 4 is replaced by a fictitious steady isentropic nozzle that converges from the passage area to the partially opened area. A guess is made of the pressure at the entrance to the nozzle. This pressure and the conditions of the first cell determine the state across the single characteristic wave traveling into the passage, and thus, the mass flux out of the passage. A second mass flux can be computed from this state, the port static pressure, and the throat area of the nozzle. These two mass flows must agree or the initial guess at the upstream nozzle pressure was incorrect. Again, the process is iterative. Upon convergence, the state at the nozzle entrance is assigned to the image cell.

III. Experimental Comparison

There are three wave-rotor experiments with which the numerical model has been compared. Two of them were performed some time ago in the 1960s.[7,8] The third experiment is presently ongoing.[9] Of the two earlier experiments, Ref. 7 was a so-called divider cycle in which air enters the rotor at some intermediate pressure, is split, and exits through two ports. In one port the stagnation pressure is higher than the entering stream and in the other it is lower. The Ref. 8 experiment was an actual wave engine (i.e., wave-rotor with heat addition). Here, air enters the rotor at a relatively low pressure and temperature, is compressed, and exits the rotor. It is then heated by an external combustor and sent back into the rotor where it is expanded and exits at a stagnation pressure and temperature above the entering cool stream. The Ref. 9 experiment is also a divider cycle; however, the details of the wave timing are quite different from those of Ref. 7.

The relative rotor geometries and parameters for the three experiments are shown in Fig. 5 and in Table 1, respectively. A quick glance at Fig. 5 shows the large differences in the passage cross sections for the three experiments.

For any of these cycles (port timing and boundary conditions) the model was run continuously until the wave pattern in the passage repeated itself, the net mass flow rate through all of the ports was zero, the cavity states were constant, and the wall temperature distribution was unchanging. Global quantities such as mass flow and outflow port stagnation values were obtained from the model by numerically integrating the mass momentum and energy flux in the image cells as they passed through the port areas. A constant area mixing calculation was then used to obtain averaged quantities.[6] All numerical calculations were performed using a nondimensional cell spacing of $\Delta x = 0.02$ and a nondimensional time step of $\Delta t = 0.007$–0.008.

A. Reference 9 Experiment

This experiment is highly instrumented, and a significant amount of data can be collected for comparison purposes.

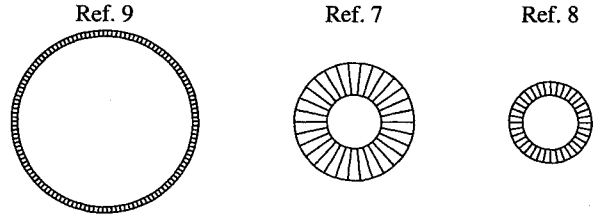

Fig. 5 Experimental rotor geometries.

Table 2 Leakage gaps of Ref. 9 experiment

δ_{leak}, cm	High leakage	Low leakage
Left wall	0.063	0.013
Right wall	0.036	0.013
Medium port	0.025	0.013
Low port	0.025	0.013
High port	0.025	0.013

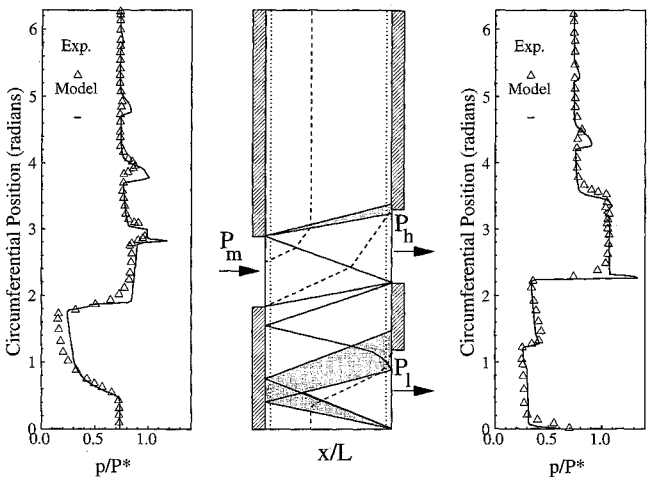

Fig. 6 Pressure trace of Ref. 9 experiment test point.

The rotor was specifically designed to parametrically study the loss mechanisms dealt with in this article. At the time of this writing, very few of the planned experimental runs have been performed. Nevertheless, the data available, combined with that of the other experiments to be compared, provide a fairly complete validation of the model.

For each experimental run all of the data necessary to the model was available. The static pressures needed for the model outlet ports were obtained using an average of 10 evenly spaced static taps in the ports of the experiment. For the configuration described in the first column of Table 1 two experimental runs were compared corresponding to two different settings of the leakage gap δ_{leak}. These settings are shown in Table 2. For each run, the ratio of high-pressure port mass flow to total mass flow β was held at a constant nominal value of 0.37. The model parameters α and C_D were found by matching both β and the cavity pressure to the experiment at two test points of the high-leakage gap run corresponding to the highest and lowest values of mass flow. It is interesting to note that the values of these two parameters varied little between the three experiments.

Figure 6 shows a comparison between model and experiment of the pressure at two axial locations onboard the passage as it moves through the cycle at one test point (maximum mass flow) of the high-leakage run. Solid lines represent the calculated pressures in the 2nd and 49th computing cells, triangles represent experimental data that was digitized from an oscillogram photograph. The wave diagram in the center of the figure shows schematically the intended cycle. Also shown in this diagram as dotted lines are the locations of the pressure transducers used to collect the data (2.5% from each end of the passage). The subscripts m, h, and l on the diagram refer to the medium- (inlet), high-, and low-pressure ports, respectively. The dashed line represents a hypothetical particle path that separates the compressed from the expanded gas. The data has been normalized by the reference pressure $P^* = 30.25$ psia. The agreement appears quite good with the only significant discrepancy being on the left side of the rotor in the vicinity of the initial expansion (1–2 rad). This region is where the pressure in the device is the lowest and the leakage gap the largest. Thus, the error may reflect the rather crude nature of the leakage model. This explanation has been verified by comparisons of the low-leakage gap cases (not shown here) that do not exhibit the discrepancy. It is reassuring that the model nicely tracks the weak waves that remain in the top portion of the cycle due to mistimed ports. Although space does not permit it, it is noted that plots similar to Fig. 6 were generated at other test points with similar agreement.

Figure 7 shows a comparison of the high- vs low-stagnation pressure for the test runs. The experimental stagnation values were obtained by a simple average of four stagnation probes placed in each port. In the figure, all of the data has been normalized by the inlet stagnation pressure. The model agreement with the data is again quite good.

Figure 8 shows a comparison of the mass flow through the device as a function of the pressure ratio P_l/P_m for the same test runs as the previous figure. The model and experiment agree well for the high-leakage case except at the lowest values of pressure ratio. For the high-leakage test points, the predicted mass flow was an average of 7% above the measured. For the low-leakage case the discrepancy was larger at an average value of 17%. One explanation for the general tendency of the model to overpredict the mass flow is that the walls of the passages have a finite thickness that creates a certain degree of blockage that is not accounted for by the model. In this experiment, e.g., the passage walls occupy approximately 16% of the total passage width. As for the difference in error between the high- and low-leakage runs, this may simply be the result of improperly chosen values of α and C_D in Eqs. (9) and (13).

Finally, Fig. 9 shows three sets of pressure contours in the wave-rotor passage that were calculated by the model. All of

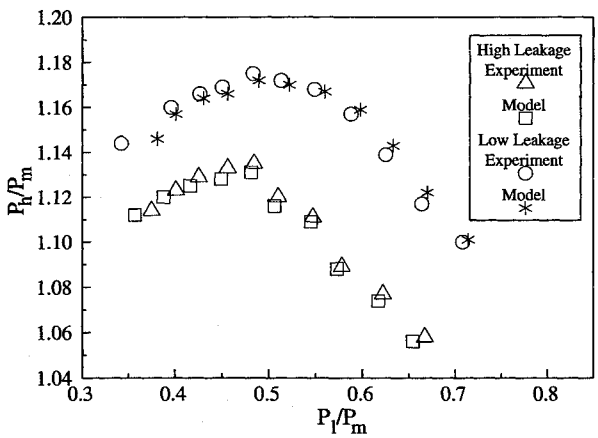

Fig. 7 Ref. 9 experiment high- vs low-pressure comparison.

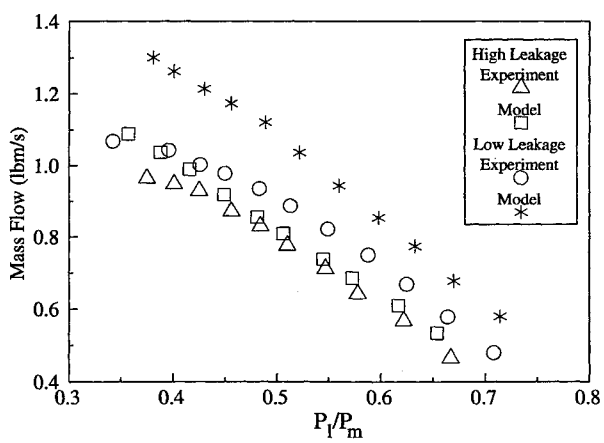

Fig. 8 Ref. 9 experiment mass flow vs low-pressure comparison.

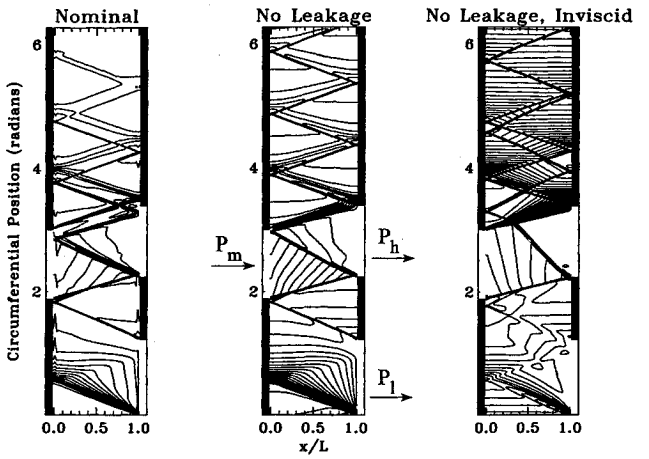

Fig. 9 Pressure contours for one Ref. 9 test point.

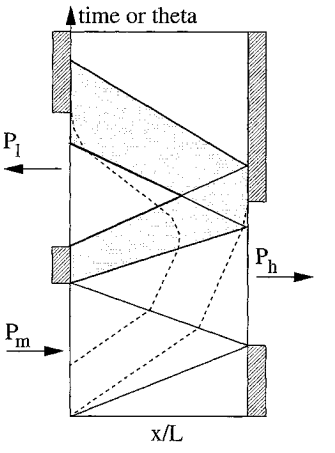

Fig. 10 Ref. 7 experimental wave diagram.

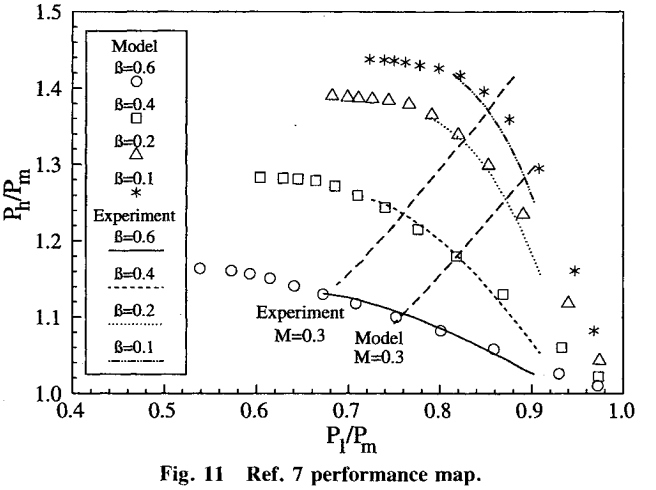

Fig. 11 Ref. 7 performance map.

the contours used the same boundary conditions from a single test point. This was the same test point used in Fig. 6. The left-most contour includes all of the loss mechanisms described above (nominal). The center contour includes only friction and heat transfer (no leakage), and the right-most contour includes only the finite opening time effect (no-leakage, inviscid). These side-by-side contours clearly illustrate the effect that the losses have on the wave pattern. Comparing first the nominal and no-leakage contours, it appears that, among other things, leakage has the effect of damping any waves that remain at the end of the cycle. This can be seen by examining the upper portion of the two contours. The effect of leakage on wave timing may also be seen by noting that in the nominal case, the shock separating the high-pressure port from the inlet port ($\theta = 2.24$–3.0 rad) arrives early, whereas in the no-leakage case it arrives at the proper time (i.e., at the closing of the port). This figure highlights the importance of including leakage effects in the model as a source term rather than attempting to compute the wave pattern without leakage and adding the effect in later to the overall performance predictions as was done in Refs. 5 and 8. Comparing the no-leakage contour to the no-leakage, inviscid contour illustrates the substantial effect that friction has on the wave timing. In particular, the waves in the inviscid calculation are quite mistimed in the high-pressure region of the cycle. The predicted mass flows from the no-leakage and no-leakage, inviscid calculations were 21 and 54%, respectively, above the base calculation with all of the losses modeled. The values of β were, respectively, 0.44 and 0.72 as compared with 0.37 for the base case.

B. Reference 7 Experiment

As mentioned, the Ref. 7 experiment was also a pressure divider; however, the port placement was quite different from Ref. 9 as was the geometry of the rotor (see Table 1). In particular, the ratio δ_{leak}/h [see Eq. (13)] was comparatively small and the passage opening time was large. Furthermore, the wave diagram, which is shown schematically in Fig. 10, was also quite different. Note that the wave diagram shown represents only one-third of a revolution of the rotor.

The comparison of model vs experiment may be summarized on the single plot shown in Fig. 11. Like Fig. 7, this is a plot of high- vs low-stagnation pressure, normalized by the inlet stagnation pressure. In this plot, however, there are several families of curves representing various values of the ratio of high-pressure port mass flow to total mass flow β. The symbols represent results from the model while the various lines represent experimental data. In the experiment, the low-pressure outlet port was vented through a flow meter to the atmosphere. It was indicated in Ref. 7 that the static pressure in this port remained nearly constant throughout the testing at approximately atmospheric pressure. Therefore, for the numerical experiment, the low-pressure port was maintained at this value. The data points were obtained by adjusting the inlet stagnation, and high-pressure outlet static pressures until the desired value of β was obtained. The inlet stagnation temperature and rotational speed were held at the constant values shown in Table 1. The comparison between the experimental and model data is good. Note, in particular, that as the low pressure is decreased more and more, indicating increased work extraction from the flow, the subsequent gain in the high pressure, indicating work done on the flow, is less and less (i.e., the curves "flatten" as one moves to the left). This trend appears to be a result of the losses, as it is not seen when they are neglected.[6] The fact that the model tracks this trend well for all values of β is particularly encouraging. Two dashed lines are also shown on this plot representing calculated and measured constant inlet Mach number lines for $M = 0.3$. For a given set of inlet conditions, the Mach number may be considered a measure of the mass flow rate. Thus, it is seen from the plot that the model again overpredicts the device throughflow.

C. Reference 8 Experiment

Information on the Ref. 8 experiment came from three quarterly reports[8] that documented the program. None of the documented tests contained complete information regarding the results. As a consequence, some of the information supplied to the model was inferred by the author of the present article. This will be explained later. It is noted, however, that this experiment was a true wave engine (i.e., with heat addition), and thus, represents an important test point for the model.

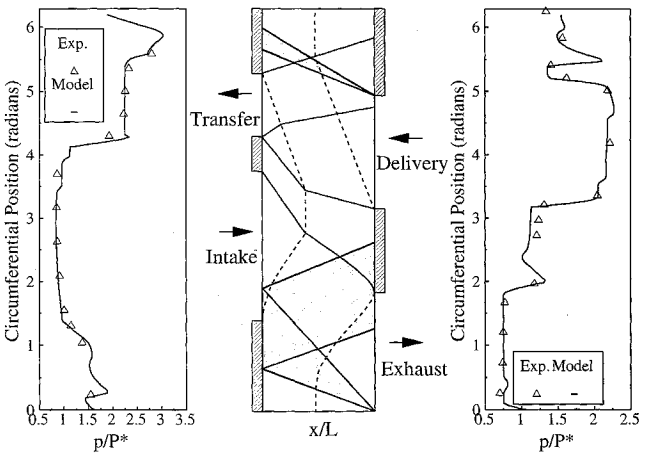

Fig. 12 Pressure trace of Ref. 8 experiment.

Figure 12 shows the proposed wave diagram and nomenclature for the cycle. The experimental data did not include stagnation pressures for the delivery port (the port coming from the burner), and so the model was modified to include a combustor. As with the rotor cavity, the combustor was treated as a single lumped capacitance system that was updated once per rotor revolution or cycle. The governing equations may be written in nondimensional form as

$$\rho_{\text{comb}}^{t+t_{\text{cycle}}} = \rho_{\text{comb}}^{t} + \left(\frac{RhL}{V_{\text{comb}}}\right)\Delta t\theta_{\text{cycle}}\left(\sum_{n=t_{\text{do}}/\Delta t}^{t_{\text{dc}}/\Delta t}[F_1]_N^n - \sum_{n=t_{\text{to}}/\Delta t}^{t_{\text{tc}}/\Delta t}[F_1]_0^n\right) \tag{19}$$

$$p_{\text{comb}}^{t+t_{\text{cycle}}} = p_{\text{comb}}^{t} + \left(\frac{RhL}{V_{\text{comb}}}\right)\theta_{\text{cycle}}(\gamma - 1) \times \left\{\gamma\Delta t\left(\sum_{n=t_{\text{do}}/\Delta t}^{t_{\text{dc}}/\Delta t}[F_3]_n^n - \sum_{n=t_{\text{to}}/\Delta t}^{t_{\text{tc}}/\Delta t}[F_3]_0^n\right) + \frac{\dot{Q}}{p^*\omega RhL}\right\} \tag{20}$$

where the subscripts do, dc, to, and tc refer to the delivery port opening and closing times, and transfer port opening and closing times, respectively. The term $\dot{Q}$ in Eq. (20) is the rate of heat addition in the combustor. The combustor pressure and temperature were used as stagnation boundary conditions for the delivery port.

Figure 12 shows a comparison, for a single test point, between the model predictions and a series of pressure taps that were placed in the endwalls or ports of the wave-rotor at various circumferential locations. The data has been scaled by the reference pressure, $P^* = 14.7$ psia. Data from the model was obtained from the image cells at either end of the passage. For this calculation, a value of $\gamma = 1.365$ was used, which is roughly equal to the mean value of the intake port and the exhaust port. The viscosity used in the model was also an average of these two states. The amount of heat added to the model combustor was adjusted until the ratio of exhaust to intake stagnation temperature matched the experiment. The agreement is excellent and it is noted that the ratio of exhaust to inlet stagnation pressure predicted by the model matched the experiment exactly.

IV. Conclusions

A numerical model has been developed that can predict the performance of a wave-rotor, given the geometry and boundary conditions. The model accounts for the important loss mechanisms of viscosity, heat transfer, leakage, and finite opening time. Comparison between the model and three geometrically different wave-rotor experiments have yielded favorable results.

Acknowledgments

The author would like to thank Jack Wilson, who designed and is currently running the NASA wave-rotor experiment, for (among other things) providing me with excellent data despite numerous unforseen difficulties in the test cell.

References

[1]Foa, J. V., *Elements of Flight Propulsion*, Wiley, New York, 1960.

[2]Kentfield, J. A. C., *Nonsteady One-Dimensional Internal Compressible Flows: Theory and Application*, Oxford Univ. Press, Oxford, England, UK, 1993.

[3]Azoury, P. H., *Engineering Application of Unsteady Fluid Flow*, Wiley, New York, 1992.

[4]Gyarmathy, G., "How Does the Comprex® Pressure-Wave Supercharger Work?," Society of Automotive Engineers Paper 830234, Feb.–March 1983.

[5]Taussig, R. T., "Energy Exchanger Performance and Power Cycle Evaluation—Experiments and Analysis," Final Rept., Dept. of Energy, DOE/ER/01084-T1, April 1980.

[6]Paxson, D. E., "A General Numerical Model for Wave-Rotor Analysis," NASA TM 105740, April 1992.

[7]Kentfield, J. A. C., "An Examination of the Performance of Pressure Exchanger Equalizers and Dividers," Ph.D. Dissertation, Univ. of London, London, 1963; also *Journal of Basic Engineering*, Vol. 91, Series D, No. 3, 1969, pp. 361–370.

[8]Klapproth, J. F., "Wave Engine Project," General Electric Quarterly Repts., R60FPD284, R60FPD419, RF60FPD585, April–Oct. 1960.

[9]Wilson, J., and Fronek, D., "Initial Results from the NASA-Lewis Wave-Rotor Experiment," AIAA Paper 93-2521, July 1993.

[10]Welch, G., "Two-Dimensional Numerical Study of Wave-Rotor Flow Dynamics," AIAA Paper 93-2525, July 1993.

[11]Larosiliere, L., "Three-Dimensional Numerical Simulation of Gradual Opening in a Wave-Rotor Passage," AIAA Paper 93-2526, July 1993.

[12]Eidelman, S., "The Problem of Gradual Opening in Wave Rotor Passages," *Journal of Propulsion and Power*, Vol. 1, No. 1, 1985, pp. 23–27.

[13]Paxson, D. E., "An Improved Numerical Model for Wave-Rotor Design and Analysis," AIAA Paper 93-0482, Jan. 1993; also NASA TM 105740, Jan. 1993.

[14]Roe, P. L., "Characteristic Based Schemes for the Euler Equations," *Annual Review of Fluid Mechanics*, Vol. 18, 1986, pp. 337–365.

[15]Holman, J. P., *Heat Transfer*, 5th ed., McGraw–Hill, New York, 1981.

[16]Kays, W. M., and Crawford, M. E., *Convective Heat and Mass Transfer*, McGraw–Hill, New York, 1980.

[17]Egli, A., "The Leakage of Steam Through Labyrinth Seals," *Transactions of the American Society of Mechanical Engineers*, Vol. 57, 1935, pp. 115–122.